Progress In Electromagnetics Research, Vol. 142, 523–544, 2013

HP-FEM AND PML ANALYSIS OF PLASMONIC PARTICLES IN LAYERED MEDIA

Mengyu Wang[1, *], Kersten Schmidt[2], Aytaç Alparslan[1], and Christian Hafner[1]

[1]Laboratory for Electromagnetic Fields and Microwave Electronics, ETH Zurich, CH-8092, Switzerland

[2]Technical University Berlin, Strasse des 17. Juni 136, Berlin D-10623, Germany

Abstract—In this paper, we introduce a high order finite element (FEM) implementation using perfectly matched layer (PML) for the scattering by plasmonic structures inside layered media. The PML is proven to be very accurate and efficient by a comparative analysis with a commercial FEM software and the Multiple Multipole Program (MMP). A convergence analysis using *hp*-adaptive refinement inside the PML layer shows that adaptive mesh refinement inside the PML layer is most efficient. Based on this convergence analysis an *hp*-strategy is proposed, which shows a remarkable error reduction for small additional computational costs.

1. INTRODUCTION

The advancing fabrication techniques in nano-technology make them more and more popular in studying structures with the size of optical wavelengths or even less. Many applications, such as nano antennas [1, 2], photonic crystals [3], and chemical and biological sensors [4–6], are usually mounted on or embedded in layered media. For reasons of simplicity, the impact of the substrate or multilayer structure on optical antennas is often ignored in simulations — as it had been traditionally done for radio frequency (RF) antennas. While RF antennas often are surrounded in air using holder that have almost no impact on the antenna, optical antennas may be strongly affected by the underlying substrate or multilayer structures.

Received 14 August 2013, Accepted 7 September 2013, Scheduled 17 September 2013

* Corresponding author: Mengyu Wang (Mengyu Wang).

In such structures we find guided and leaky waves [7] which are not present in homogeneous exterior of scattering objects. The Sommerfeld radiation condition [8, 9] decides, in homogeneous exterior, if a wave is outgoing or incoming, and guarantees, in this way, a unique definition of purely outgoing scattered fields. Several conditions have been proposed to replace or extend the Sommerfeld radiation condition to multilayer structures (see, e.g., [10–15]).

For the numerical analysis of scattering problem in unbounded multilayer structures, the most important issue is the truncation of the domain. Boundary integral methods [16], which are based on Green's functions for each piecewise constant subdomain, are most powerful for the handling of the scattering in homogeneous unbounded domains. The direct application to layered structures has to face the problem of infinite interfaces. With the development of integration techniques for the evaluation of multilayer Green's functions [15, 17], formulations on only the boundary of the scatterer are possible, and such a formulation has been successfully used with MMP [18]. For homogeneous exterior, there are a variety of local absorbing boundary conditions [8, 9] which can be used with volume discretization methods such as FEM or the finite difference time domain method (FDTD). The perfectly matched layers (PML), which is the most popular truncation technique, was first proposed in [19] and later introduced to FEM [20]. The introduction of PML can be considered as a complex coordinate stretching [21], which leads to exponentially decaying solutions. In FDTD, the geometry of the PML is naturally rectangular due to the structured mesh of FDTD. In 2D FEM, the typical shapes of PML blocks are rectangles and circular shells, which correspond to Cartesian [22] and radial PML [23], respectively. Motivated by the pole condition, PML have also been proposed for more general layered media [24]. To reduce the error, the thickness and mesh widths in the PML can be *a-posteriori* adapted [25–28]. The Hardy space infinite elements [29] and the pole condition method [30, 31] are alternative methods for multilayer structures.

In this article, the modeling of multilayer scattering in the presence of guided modes is studied using FEM with an *hp*-adaptive PML discretization. The possibility to refine the mesh (h-refinement), to increase the polynomial order (p-refinement) or both (hp-refinement) even only in certain parts of the mesh (adaptive refinement) allows well-adapted refinement strategies [32]. Using those strategies, an error level can be reached with much lower number of degrees of freedom (DOF) than with uniform mesh refinement and constant polynomial degree. For wave propagation, it is known that p-refinement is superior to h-refinement, at least away from material corners [33–35]. Close to material corners, the use of geometric meshes and a linear

increase of the polynomial orders away from these corners lead to exponential convergence [36], see also [37] in the application of photonic devices. Using error estimators adaptive refinement strategies has been proposed [38–45]. To the best of our knowledge, an *hp*-adaptive refinement strategy in the presence of PML has been proposed only in [27]. In this work, we study the *hp*-adaptive PML discretization of an anisotropic mesh refinement towards the PML interface or an increase of the polynomial orders.

In Section 2, we provide a variational formulation for the scattered field in multilayer structures using PML. The FEM discretization of the method is shown to be efficient to handle the scattering problem of plasmonic particles in the layered media (see Section 3). The error analysis for the *hp*-adaptive refinement of the FEM is performed in Section 4.

2. FINITE ELEMENT FORMULATION AND IMPLEMENTATION

2.1. Finite Element Variational Formulation Using PML

In this paper, we focus on two-dimensional scattering problems, where the electromagnetic waves propagate in a non-magnetic material, with the relative permittivity $\epsilon(x, y) = \epsilon(\bar{\mathrm{x}})$. Here $\bar{\mathrm{x}}$ denotes the 2D coordinates (x, y) since the problem is independent of the third coordinate z.

As usual, the electromagnetic wave (E, H) is decomposed into transverse electric (TE) waves $(E_x, E_y, 0, 0, 0, H_z)$ and transverse magnetic (TM) polarized waves $(0, 0, E_z, H_x, H_y, 0)$ [7, 46]. This decomposition leads to scalar 2D Helmholtz equations in H_z and in E_z. In the optical regime, a surface plasmon resonance can be excited if a noble metal is illuminated by a TE wave [47]. It should also be noted that according to recent research, another low-energy collective mode can be excited as well [48–53]. We consider TE waves with magnetic polarization $\bar{\mathrm{H}}(\bar{\mathrm{x}}) = (0, 0, u^{\mathrm{tot}})$, where u^{tot} denotes the total magnetic field, and we denote by k_0 the wave number of the impinging wave $\bar{\mathrm{H}}^{\mathrm{imp}}(\bar{\mathrm{x}}) = (0, 0, u^{\mathrm{imp}})$ from above.

For reasons of simplicity, we consider a plasmonic object within a multilayer structure as test case, which is illustrated in Figure 1. The multilayer structure is defined in $\mathbb{R}^2$ through its piecewise constant relative permittivity $\epsilon_{\mathrm{mul}}(\bar{\mathrm{x}})$ only varying in y direction. The permittivity ϵ_{mul} takes the values ϵ_{lay} in the substrate, ϵ_{coat} in coatings of the substrate to the top and bottom and 1.0 in the air region above and below the coatings. Inside the substrate lies the scatterer Ω_{sc} with relative permittivity ϵ_{sc} and boundary Γ, and we define the overall

permittivity $\epsilon(\bar{\mathrm{x}})$ to coincides with $\epsilon_{\mathrm{mul}}(\bar{\mathrm{x}})$ outside the scatterer and with ϵ_{sc} inside the scatterer.

We are going to use a *scattered field formulation*, in which the scattered field u^{sc} in the decomposition $u^{\mathrm{tot}} = u^{\mathrm{sc}} + u^{\mathrm{inc}}$ is the unknown. For this we have to define a generalized incoming field $\bar{\mathrm{H}}^{\mathrm{inc}} = (0, 0, u^{\mathrm{inc}})$ which solves

$$-\nabla \cdot \left(\frac{1}{\epsilon_{\mathrm{mul}}(\bar{\mathrm{x}})} \nabla u^{\mathrm{inc}} \right) - k_0^2 u^{\mathrm{inc}} = 0 \tag{1}$$

in the whole space $\mathbb{R}^2$. Its incoming part from above is the impinging wave $\bar{\mathrm{H}}^{\mathrm{imp}}$, and it is purely outgoing to the bottom. This generalized incoming field u^{inc} consists of the reflected and transmitted wave in each layer and can be computed analytically [7].

Then, the scattered field u^{sc} solves

$$-\nabla \cdot \left(\frac{1}{\epsilon_{\mathrm{mul}}(\bar{\mathrm{x}})} \nabla u^{\mathrm{sc}} \right) - k_0^2 u^{\mathrm{sc}} = 0 \quad \text{in } \mathbb{R}^2 \setminus \Omega_{\mathrm{sc}} \tag{2a}$$

$$-\nabla \cdot \left(\frac{1}{\epsilon_{\mathrm{sc}}} \nabla u^{\mathrm{sc}} \right) - k_0^2 u^{\mathrm{sc}} = \left(1 - \frac{\epsilon_{\mathrm{lay}}}{\epsilon_{\mathrm{sc}}} \right) k_0^2 u^{\mathrm{inc}} \quad \text{in } \Omega_{\mathrm{sc}} \tag{2b}$$

$$\left[u^{\mathrm{sc}} \right]_\Gamma = 0 \tag{2c}$$

$$\left[\frac{1}{\epsilon(\bar{\mathrm{x}})} \nabla u^{\mathrm{sc}} \cdot \mathrm{n} \right]_\Gamma = \left(\epsilon_{\mathrm{sc}}^{-1} - \epsilon_{\mathrm{lay}}^{-1} \right) \partial_n u^{\mathrm{inc}}, \tag{2d}$$

and is purely outgoing to all sides. Here, $[\cdot]_\Gamma$ stands for the jump between field values outside and inside the scatterer. As the multilayers approach infinity and the scattered field may incorporate outgoing guided modes to the left and right, which do not decay, the Sommerfeld radiation condition [8, Chap. 1, 9, Chap. 3] does not apply. On its place the outgoing nature of u can be enforced by a more general radiation conditions [10–13], the pole condition [14] or by means of the multilayer Greens functions [15, 17]. For applying the pole condition and the PML, one has to exclude guided waves with different directions of group and phase velocities, which have, however, to our best knowledge, never been found in dielectric multilayer structures.

We are interested in obtaining the scatterer field in a rectangle region of interest Ω around the scatterer Ω_{sc} (see Figure 1).

Following the standard procedure for the Galerkin method, Equation (2a) is multiplied with a test function v and integrated over Ω. After integration by parts, we obtain the equation

$$\begin{aligned} &\int_\Omega \frac{1}{\epsilon(\bar{\mathrm{x}})} \nabla u^{\mathrm{sc}} \cdot \nabla v \, \mathrm{d}\bar{\mathrm{x}} - k_0^2 \int_\Omega u^{\mathrm{sc}} v \, \mathrm{d}\bar{\mathrm{x}} - \int_{\partial\Omega} \frac{1}{\epsilon(\bar{\mathrm{x}})} \partial_n u^{\mathrm{sc}} v \, \mathrm{d}\bar{\mathrm{s}} \\ &= k_0^2 \int_{\Omega_{\mathrm{sc}}} \left(1 - \frac{\epsilon_{\mathrm{lay}}}{\epsilon_{\mathrm{sc}}} \right) u^{\mathrm{inc}} v \, \mathrm{d}\bar{\mathrm{x}} + \int_\Gamma \left(\epsilon_{\mathrm{lay}}^{-1} - \epsilon_{\mathrm{sc}}^{-1} \right) \partial_n u^{\mathrm{inc}} v \, \mathrm{d}\bar{\mathrm{s}}. \end{aligned} \tag{3}$$

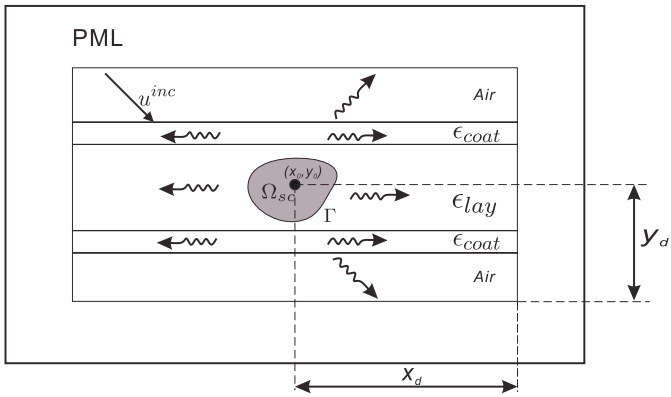

Figure 1. Scattering from the multi-layered test structure, illuminated by a plane wave from top. Scattered and guided waves can be excited. The physical domain is surrounded by a PML.

This equation is not complete, since no boundary conditions are specified. Therefore, we enlarge the computational domain by a PML layer. By applying the PML coordinate transformation, one can obtain the variational formulation in the whole computational domain $\Omega_0 := \Omega \cup \Omega_{\text{PML}}$, which is a box-shaped domain for the Cartesian PML. The details of the transformation can be found in [22].

The transformation leads to a transformed scattered field outside Ω, which exponentially decays away from the PML interface $\partial\Omega$ and is almost zero on $\partial\Omega_0$, if the PML layer is thick enough. Therefore, we neglect the corresponding boundary term on $\partial\Omega_0$ corresponding to homogeneous Neumann boundary conditions. The unknown of the resulting variational formulation u shall be an approximation to u^{sc} in Ω and exponentially decaying in Ω_{PML}. Then, the problem reads:

$$\text{find } u \in H^1(\Omega_0), \text{ s.t. } \Phi_0(u,v) = f(v), \quad \text{for all } v \in H^1(\Omega_0), \tag{4}$$

where

$$\Phi_0(u,v) = \int_{\Omega_0} \nabla u^T \,\overline{\overline{\text{A}}}(\bar{\text{x}}) \nabla v \,\text{d}\bar{\text{x}} - k_0^2 \int_{\Omega_0} b(\bar{\text{x}}) uv \,\text{d}\bar{\text{x}}$$

$$f(v) = \int_{\Omega_{\text{sc}}} \left(1 - \frac{\epsilon_{\text{lay}}}{\epsilon_{\text{sc}}}\right) k_0^2 u^{\text{inc}} v \,\text{d}\bar{\text{x}} + \int_{\Gamma} \left(\epsilon_{\text{lay}}^{-1} - \epsilon_{\text{sc}}^{-1}\right) \partial_n u^{\text{inc}} v \,\text{d}\bar{\text{s}},$$

and

$$\overline{\overline{\text{A}}}(\bar{\text{x}}) = \begin{pmatrix} \frac{\gamma_y(y)}{\gamma_x(x)} \frac{1}{\epsilon(\bar{\text{x}})} & 0 \\ 0 & \frac{\gamma_x(x)}{\gamma_y(y)} \frac{1}{\epsilon(\bar{\text{x}})} \end{pmatrix}$$

$$b(\bar{\text{x}}) = \gamma_x(x)\gamma_y(y)$$

$$\gamma_x(x) = 1 + i\sigma_x(x)/\omega$$
$$\gamma_y(y) = 1 + i\sigma_y(y)/\omega$$
$$\sigma_x(x) = \begin{cases} 0, & \text{if } |x - x_0| - x_d \leqslant 0, \\ S_x \left(|x - x_0| - x_d\right)^{\alpha_x}, & \text{if } |x - x_0| - x_d > 0, \end{cases}$$
$$\sigma_y(y) = \begin{cases} 0, & \text{if } |y - y_0| - y_d \leqslant 0, \\ S_y \left(|y - y_0| - y_d\right)^{\alpha_y}, & \text{if } |y - y_0| - y_d > 0. \end{cases}$$

Note that the boundary term $\int_{\partial\Omega} \frac{1}{\epsilon(\bar{\mathrm{x}})} \partial_n uv \, \mathrm{d}\bar{\mathrm{s}}$ disappears due to the continuity at the PML interface $\partial\Omega$.

In the formulation, (x_0, y_0) is the center of the computational domain, and x_d, y_d are the distances of the PMLs from the center in x and y directions. The geometrical configuration of the PML is shown in Figure 1. The functions σ_x and σ_y describe the profile of the PML. They are monotonic polynomial functions in x and y inside the PML region, where the constants S_x, S_y are the amplitudes, and α_x, α_y are the polynomial orders of the profiles. The profiles play a key role for the performance of PML. Nowadays it is accepted that the profile functions σ_x and σ_x should be continuous over the PML interface, which leads to the continuity of the first derivative of u, as well as their first derivative such that the second derivative of u is continuous as well. Hence, we choose α_x, $\alpha_y \geq 2$.

Furthermore, the combination of S_x, S_y and α_x, α_y must be chosen carefully. Greater S_x, S_y provides better absorption and decreases the modeling error but also leads to more rapid decay of the field in the PML and needs more effort for the discretization. The stronger the PML absorption is, the more computational effort is required.

2.2. CONCEPTs Implementation

For the discretization of (4), we use the C++ library `CONCEPTs` [37, 54, 55]. The `CONCEPTs` package uses high polynomial basis functions and curved quadrilateral elements. In `CONCEPTs`, the polynomial order can be chosen independently in each cell. Hence, we can use the library for adaptivity in the mesh width as well as the polynomial order. All the integrals in the formulation can be implemented in `CONCEPTs`, and the corresponding relationships are shown in Table 1.

`CONCEPTs` requires quadrilateral curvilinear elements. For obtaining an appropriate mesh of the structure, we applied the mesh generator EZ4U [56, 57] for a small rectangular box including the scatterer, which generates quadrilateral curvilinear elements with good quality, as shown in Figure 2(a). This mesh describes the details of the curved scatterer. Difference from FE methods based on straight

Table 1. The implementation of the integrals in `CONCEPTs`.

integral	`CONCEPTs` class	symbol	type
$\int_\Omega \nabla u^T \overline{\overline{\mathrm{A}}}(\bar{\mathrm{x}}) \nabla v \, \mathrm{d}\bar{\mathrm{x}}$	hp2D::Laplace	$\mathcal{S}$	stiffness matrix
$\int_\Omega b(\bar{\mathrm{x}}) uv \, \mathrm{d}\bar{\mathrm{x}}$	hp2D::Identity	$\mathcal{M}$	mass matrix
$\int_\Gamma fv \, \mathrm{d}\bar{\mathrm{s}}$	hp1D::Riesz	f_Γ	load vector
$\int_{\Omega_{\mathrm{sc}}} gv \, \mathrm{d}\bar{\mathrm{x}}$	hp2D::Riesz	$\mathsf{f}_{\Omega_{\mathrm{sc}}}$	load vector

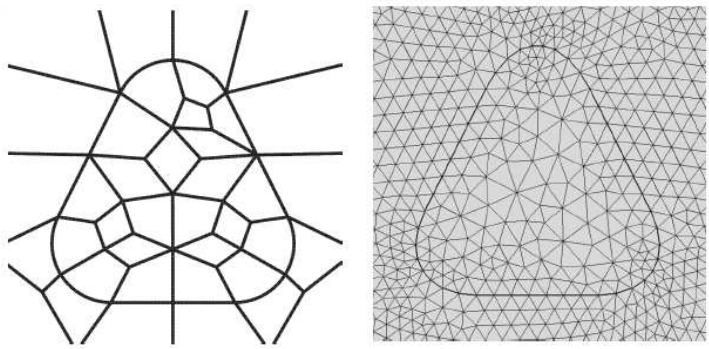

Figure 2. `CONCEPTs` and COMSOL meshes near the scatterer. (a) The `CONCEPTs` mesh using quadrilateral elements generated by EZ4U. (b) The COMSOL mesh using triangular elements.

triangular or quadrilateral cells where a fine mesh is required to resolve the material interface, we may use coarse cells as the circular curved obstacle is exactly resolved by the mesh.

3. NUMERICAL SIMULATIONS

In this section, we aim to apply the introduced FE formulation with PML to two examples and to verify the accuracy of the simulation by a comparison with results using a MMP code with multilayer Greens's functions. To show the efficiency of using high-order finite elements for multilayer scattering problems using PML, we compare our implementation in the high-order FEM library `CONCEPTs` with the commercial FE program COMSOL.

3.1. Testing Problems

As shown in Figure 1, we compute the scattering of a plane wave at a silver scatterer embedded in a three-layer medium. All the layers extend towards infinity in horizontal direction. The center layer, with thickness 350 nm and relative permittivity ϵ_{lay}, is coated with two 50 nm-thick layers with relative permittivity ϵ_{coat}. A TE-polarized plane wave impinges from top with a 45 degree angle of incidence. The wavelength of the plane wave is 600 nm, at which the relative permittivity of silver ϵ_{Ag} is $-15.855 + 0.432i$ [46]. With certain combinations of ϵ_{lay} and ϵ_{coat}, guided wave modes can be excited in the coating layers. As our test problem, we choose the relative permittivities $\epsilon_{\text{lay}} = 4$ and $\epsilon_{\text{coat}} = 9$. It should be noted that the geometry analyzed here has three guided waves observed for TE polarization, with the following wave numbers: $k_{gw1} = 1.21k_0$, $k_{gw2} = 1.77k_0$ and $k_{gw3} = 1.97k_0$, where $k_0 = \frac{\omega}{c}$ is the wave number in vacuum.

We simulate two shapes of scatterers. One is a disk of radius 100 nm, and the other is an isosceles triangle with bottom length of 160 nm and height of 160 nm. The triangle has curved corners with radii of 30 nm and is shown in Figure 2. Both scatterers are embedded in the middle of the center layer.

3.2. Modelling Parameters and Numerical Results

For the simulations with the proposed formulation and using `CONCEPTs`, we choose the box with $x_d = 800$ nm and $y_d = 550$ nm as domain of interest and add a PML layer of 100 nm thickness in both x and y directions. The PML profiles are parabolic curves with parameters $S_x = S_y = 0.2$, and $\alpha_x = \alpha_y = 2$.

Coarse meshes around the scatterers are generated by EZ4U. This mesh has 27 cells for the disk and 49 cells for the triangle (see Figure 2(a)). For the multilayers and PML layer, a Cartesian mesh is added to obtain combined mesh with 191 cells for the disk and with 205 cells for the triangle. We use a uniform polynomial degree of 14 resulting in 22,741 DOFs for the circular scatterer and 21,876 DOFs for the triangular one. The absolute values of the total magnetic fields are shown in Figure 3(a) for the disk and in Figure 3(b) for the triangle. The excited guided waves are observed in the layers. With the used simulation parameters, one observes almost no artificial reflection by the PML layer. The PML has very good absorption when truncating the layers containing strong guided waves.

To verify the simulation with the proposed formulation, OpenMaX, an open source electromagnetic simulation tool that

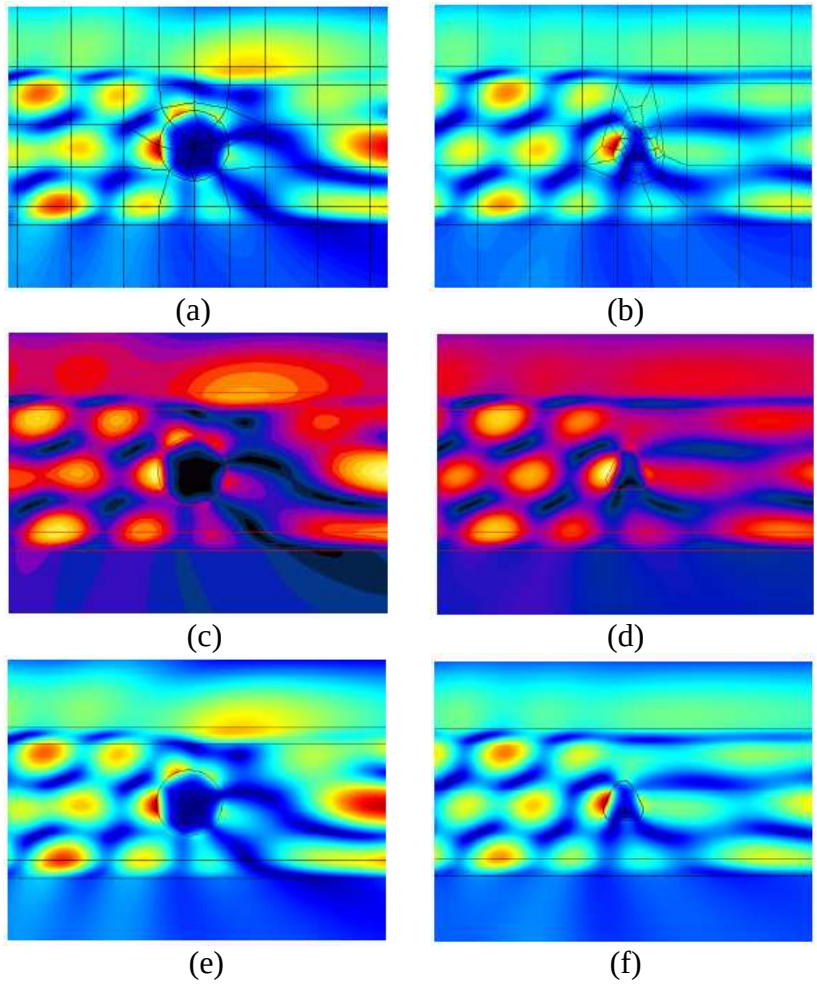

Figure 3. Simulation results for the absolute value of the total magnetic field. In (a), (c) and (e) the results for circular scatterer are shown, and (b), (d) and (f) the results for triangular scatterer. The results with `CONCEPTs` are in (a), (b), where we use a polynomial degree of 14 resulting in 22,741 DOFs for the disk, and 21,876 DOFs for the triangle. (c), (d) show the MMP results. For the disk, 64 layered expansions and a Bessel expansion with the maximum order of 30 are used. For the triangle, 51 multilayer expansions are used inside the scatterer and 23 homogeneous media multipoles are used outside the scatter. (e), (f) COMSOL results using quadratic elements, where 155,798 DOFs are used for the disk and 177,477 DOFs for the triangle.

includes the Multiple Multipole Program (MMP), is used. MMP is a boundary discretization method that uses a set of fundamental solutions of Maxwell's equations (multipole expansions) in order to obtain the fields scattered by objects [18, 58–60]. Inside the scatterer, an expansion with Bessel functions or multipoles of different centers is used, whereas in the multiple layers the solution is expanded in multilayer Green's functions with different centers. For the circular scatterer, 64 multilayer Green's functions and a Bessel expansion with the maximum order of 30 are used. Solutions are obtained with the average field mismatch error criterion of 0.001% checked in 256 matching points distributed linearly on the scatterer. For the triangular scatterer, 51 multilayer Green's functions and 23 homogeneous media multipoles with the maximum order 3 are used. The problem is solved by using 150 matching points with the average mismatch error of 0.02%. The absolute values of the total magnetic fields are shown in Figure 3(c) for the disk and in Figure 3(d) for the triangle.

We also simulated the test problem with COMSOL Multiphysics version 4.3a [61]. Under the graphical interface of COMSOL, linear, quadratic and cubic elements are available, which correspond to the 1st, 2nd and 3rd order elements, respectively. We choose quadratic and cubic elements for computation. The geometrical approximation is chosen to be 'Quintic' (5th order). Since the polynomial order two and three are rather low, we choose a very finer mesh (see Figure 2(b)) with 16,288 cells for the disk for $p = 2$, and 7,172 cells for $p = 3$, while with 9,506 cells for the triangle for both $p = 2$ and $p = 3$. For the circular scatterer, the simulation consumes 155,798 DOFs when using quadratic elements. In the simulation using cubic elements, for which a coarser mesh is applied, 141,791 DOFs are consumed. For the triangular scatterer, the simulations consume 177,477 DOFs when using quadratic elements and 229,827 DOFs when using cubic elements. Finally, the PML is configured by the default settings. The absolute values of the total magnetic fields for the performed simulations are shown in Figure 3(e) for the disk and in Figure 3(f) for the triangle, where both of the simulations use quadratic elements.

3.3. Comparisons

We compare the accuracy of the simulations with `CONCEPTs` and COMSOL in terms of the normalized absolute value of the total magnetic field $|H_{\text{tot}}|/\max(|H_{\text{tot}}|)$ along the interface of the silver disk Γ. For MMP, it is known that the accuracy is at the order of the field mismatch, so about 10^{-5}. Hence, we use the result obtained with MMP as reference. The computed fields and the differences of the

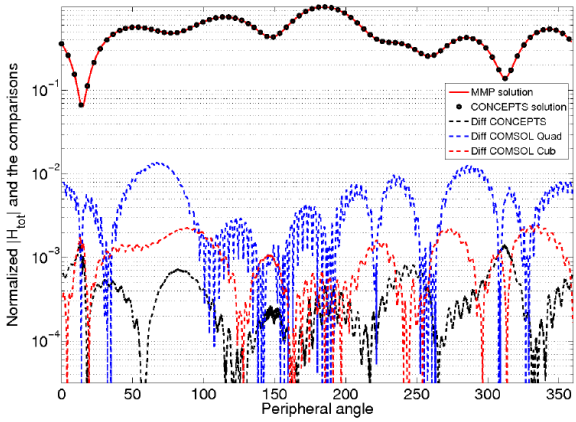

Figure 4. Comparisons for the normalized absolute value of the total magnetic field along the trace of the silver disk Γ (in logarithmic scale). The red curve represents the MMP result. The black dots represent the `CONCEPTs` result. The black dashed curve represents the difference between `CONCEPTs` and MMP results; the blue dashed curve represents the difference between MMP result and COMSOL result using quadratic elements, and the red dashed curve represents the difference between MMP result and COMSOL result using cubic elements.

`CONCEPTs` solution, the COMSOL solutions using quadratic and cubic elements to the reference solutions are shown in Figure 4. We obtain maximal errors of 1.5×10^{-3} for the `CONCEPTs` solution, and 1.4×10^{-2} and 2.4×10^{-3} for the COMSOL solutions with quadratic and cubic elements, respectively.

From the comparison, one can see the advantage of using high order elements. Compared to the quadratic elements, the cubic elements use a coarser mesh and less DOFs, while they achieve even higher accuracy. `CONCEPTs` simulation using polynomial degree 14 uses an even coarser mesh and much lower number of DOFs, where an even higher accuracy is achieved. From the comparison, one can draw the conclusion that high order FEM is more efficient for our problem.

4. *HP*-FEM ANALYSIS

Finite element methods are based on piecewise polynomial approximations of the solution of a partial differential equation, which is based on a partition of the computational domain in curvilinear cells. The

accuracy of the solution can be improved either by h-refinement, i.e., for a fixed polynomial degree p, the mesh size h is decreased, or by p-refinement, i.e., the polynomial degree p is increased for a fixed mesh size h, or a combination of both, the hp-refinement [32]. We speak about hp-adaptive FEM [32] for refinement strategies where each cell may be refined independently, and the polynomial order in each cell may be raised independently.

For the studied formulation with PML, the solutions in the domain of interest Ω and in the PML layer Ω_{PML} have different properties. We study the test example of a silver disk which was described in Section 3.2, for which we start with a coarse mesh resolving the scatterer, the interfaces of the multiple layers and the PML interface.

For this example, the solution is primarily smooth in each subdomain of different materials in the physical domain Ω. Therefore, we apply only uniform p-refinement in Ω and call p_{int} the polynomial order in these cells. For the given mesh, the polynomial order has to exceed a particular value such that the wave form can be at least coarsely resolved and that the solution converges [33–35].

The complex coordinate transformation of PML leads to exponentially decaying solutions inside the PML layer, which results in very high gradients close to the PML interface, whereas vanishing close to the outer boundary. This behavior of the solution may lead to a locking phenomena when using a uniform mesh refinement, which means that a convergence of the solution may start only for a very small mesh width. This phenomenon is weakened by the standard way of using continuous profile functions and optimized PML parameters. Motivated by the exponentially decaying solution, we are going to study a geometric mesh refinement towards the PML interface. Figure 5 illustrates this refinement strategy. The mesh in Figure 5(a) is the original mesh, which we call h_0. To obtain the refined mesh h_1 (see Figure 5(b)) from h_0, we subdivide all cells having one edge on the PML interface or its extension in the respective outer direction. In the same way, mesh h_2 (see Figure 5(c)) is obtained by another geometric refinement of mesh h_1. In general, we have a mesh h_ℓ, $\ell \in \mathbb{N}$.

The study of this adaptive mesh refinement will be in comparison to a uniform p-refinement in the PML layer, which is motivated by the fact that the decaying solution is piecewise smooth. We call p_{ext} the polynomial order of the cells in the PML layer, which may be different from p_{int}.

Hence, we characterize the hp-adaptive FEM strategy as an array of numbers $(p_{\text{int}}, p_{\text{ext}}, \ell)$. For example, (10, 8, 2) means the polynomial degrees are 10 in the physical domain and 8 in the external PML domain, and two steps of h-refinement are applied in the PML domain

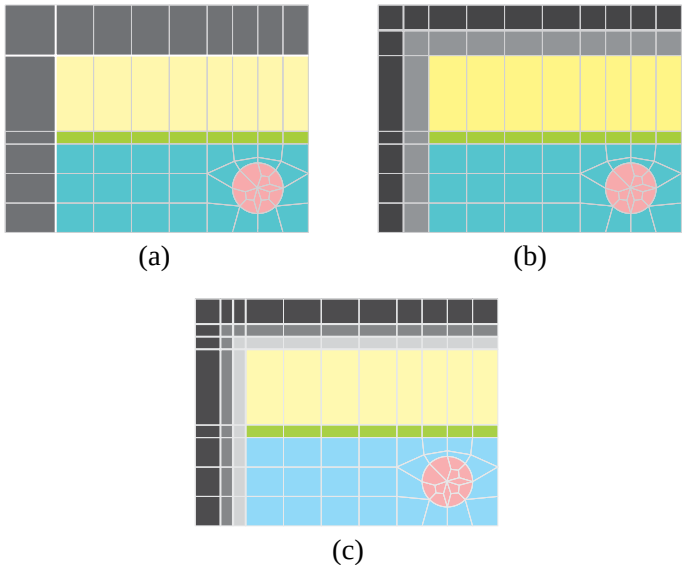

Figure 5. Adaptive h-refinement. (a) The original mesh h_0. (b) Mesh h_1, obtained by one step of h-refinement from mesh h_0. (c) Mesh h_2, obtained by one more step of h-refinement from mesh h_1.

towards the PML interface.

We start the study with $p_{\text{int}} = 8$ and $p_{\text{ext}} = 4$ on the coarse mesh h0, for which the relative L^2 error in the domain of interest is below 1. The relative L^2 error is defined as the ratio between the L^2 norm of the discretization error $u_{hp} - u_{\text{ref}}$ and the reference solution u_{ref} in the domain of interest, which reads

$$\frac{\sqrt{\int_\Omega |u_{hp} - u_{\text{ref}}|^2 d\bar{\text{x}}}}{\sqrt{\int_\Omega |u_{\text{ref}}|^2 d\bar{\text{x}}}}.$$

As reference solution we use a very fine `CONCEPTs` solution with an hp combination of (24, 24, 4). For fixed $p_{\text{int}} = 8$ we vary p_{ext} and ℓ from a combination of [4, 6, 8, 10] $\times$ [0, 1, 2, 3, 4]. For each instance of simulation, we compute the relative L^2 error and record the degrees of freedom. To see also the influence of p-refinement in the physical domain we repeat a similar set of simulations with $p_{\text{int}} = 10$ and a combination of p_{ext} and ℓ in [6, 8, 10, 12] $\times$ [0, 1, 2, 3, 4]. The results of the convergence study are illustrated in Figure 6, where the first group of simulations are shown in Figure 6(a), while the second group in Figure 6(b). In each figure, there are 20 points obtained from 20

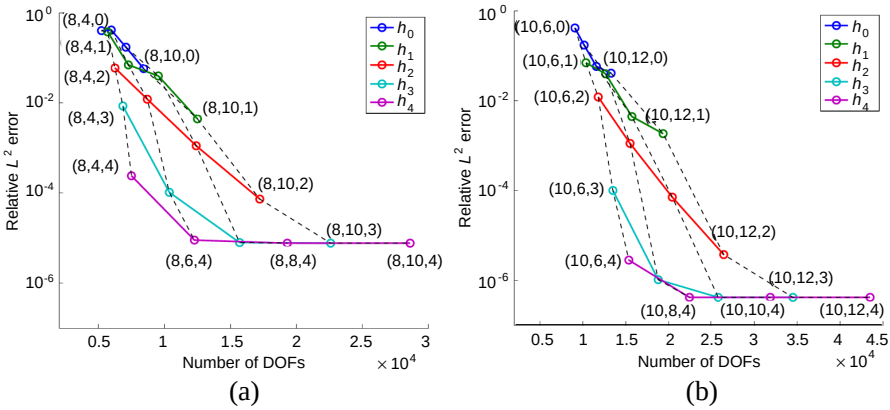

Figure 6. The *hp*-convergence analysis for the scattering problem of a silver disk. Each node represents a simulation with an *hp* combination of $(p_{\text{int}},\ p_{\text{ext}},\ \ell)$. (a) A group of 20 simulations with $p_{\text{int}} = 8$, $p_{\text{ext}} \in [4, 6, 8, 10]$, and $\ell \in [0, 1, 2, 3, 4]$. (b) A group of simulations with $p_{int} = 10$, $p_{\text{ext}} \in [6, 8, 10, 12]$, and $\ell \in [0, 1, 2, 3, 4]$. The solid lines connect the nodes with the same mesh and show the convergence with respect to p_{ext}. And the dashed lines connect the nodes with the same p_{ext} and show the convergence with respect to the mesh refinement.

instances of FEM simulations. We connect the points with the same h-refinement by solid lines, while the points with the same p_{ext} by dashed lines. The solid lines represent the p-convergence of p_{ext}, while the dashed lines represent the adaptive h-convergence.

One observes in both diagrams that the error decays if either p_{ext} is increased or the mesh refinement towards the PML interface, until a saturation level is reached, where further refinement inside the PML layer has no effect on the error. For $p_{\text{int}} = 8$ the relative error can be reduced to 9.00×10^{-6} which is reached for the *hp* combination $(8, 6, 4)$ and with $12,259$ DOFs. When the saturation level is approached, the error inside the physical domain becomes dominant, and further error reduction is only possible by increasing p_{int}. By increasing p_{int} from 8 to 10 the level of error saturation reduces by a factor of 20. An relative L^2 error of 4.16×10^{-7} is obtained for the *hp* combination $(10, 8, 4)$ with $22,465$ DOFs. Before the saturation level is reached, the error inside the PML domain dominates, therefore *hp*-refinement in the PML domain will lead to convergence to the exact solution. We observe exponential convergence above the saturation level for both p-refinement in the PML layer and the adaptive mesh refinement, whereas the mesh refinement towards the PML interface

is computationally more efficient than increasing p_{ext} — the dashed lines in Figure 6 are more steep than the solid lines. We observe that mesh refinement towards the PML interface is more adapted to the exponential decay of the solution inside the PML layer than increasing polynomial orders. For instance, starting with the *hp* combination $(8, 4, 0)$, an error level of about 10^{-4} is reached by four steps of the adaptive mesh refinement, i.e., at $(8, 4, 4)$, with $7,503$ DOFs, whereas increasing the polynomial degree p_{ext} to 10 only leads to an error of about 6×10^{-2} with $8,432$ DOFs at $(8, 10, 0)$. If we start increasing p_{ext} from *hp* combination $(8, 4, 2)$, i.e., after two steps of mesh refinement from $(8, 4, 0)$, the error drops below 10^{-4} at *hp* combination of $(8, 10, 2)$, with $17,243$ number of DOFs, which is more than two times as that for *hp* combination of $(8, 4, 4)$. Nevertheless, we expect that at a certain point it is necessary to increase p_{ext} to obtain very low error levels. It should also be noted that in case the mesh is too coarse and the polynomial orders too low, there is no error reduction by mesh refinement or by increasing the polynomial degree. For example, we also observed in our experiments that the error does not reduce if starting with *hp* combination $(8, 4, 0)$, no matter if p_{ext} is increased to 6 or one step of the adaptive mesh refinement is applied. This is due to the fact that the *hp* combination is not entering the asymptotic regime of convergence.

Having many numerical solutions with their different *hp* combinations computed, we can answer the question of optimal refinement strategies for this example, which is assured to be also applied to similar problems. We assume three refinement options:

a. increasing p_{int} by 2,
b. increasing p_{ext} by 2, and
c. one step of adaptive mesh refinement, so increasing ℓ by 1.

To expose an optimal strategy we start with an *hp* combination of $(8, 6, 0)$, which is in the asymptotic regime of convergence. Then, we compare the error reductions for the three options, and choose that with the highest error reduction for least increase of degrees of freedom and repeat the steps for this choice. In Figure 7 the optimal refinement strategy is illustrated. For the starting combination $(8, 6, 0)$ with $5,979$ DOFs an relative error of 4.05×10^{-1} is obtained. Option c is the best choice for the first four steps. Therefore, four times of *h*-refinement are performed and lead to *hp* combination of $(8, 6, 4)$. In the fifth step, the saturation is reached. Therefore, neither option b nor c will improve the solution anymore; however, option a will surpass the saturation level of p_{int} and leads to a further improvement. Thus, option a is applied, and the strategy ends at *hp* combination of $(10, 6, 4)$ with $15,389$ DOFs

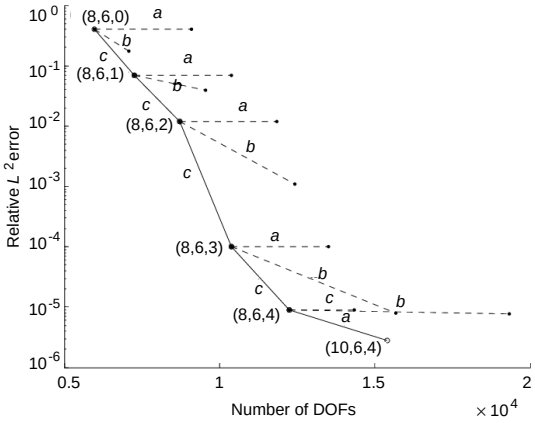

Figure 7. The *hp*-convergence strategy. Three options are represented by a, b, and c, where a means increasing p_{int} by 2, b means increasing p_{ext} by 2, and c means increasing ℓ by 1. The experiment starts at an *hp* combination of $(8, 6, 0)$ with 5,979 DOFs and an error of 4.05×10^{-1}, and stops at an *hp* combination of $(10, 6, 4)$ with 15,389 DOFs and an error of 2.83×10^{-6}.

and an error of 2.83×10^{-6}. At each step, the best choice is plotted as solid line, while the unchosen ones as dashed lines. All the steps generate a decision tree, where each node represents the optimal choice in each step, whereas dashed branches show the non-optimal choices.

5. CONCLUSIONS

In this paper, we have formulated perfectly matched layers (PML) with finite element method (FEM), for the scattering by plasmonic objects embedded in layered media. The formulation is realized using the high order FEM package `CONCEPTs`. We observe that the PML has very good absorptive behavior even in the presence of strong guided waves inside the layers. The accuracy of the simulation was validated by Multiple Multipole Program (MMP).

`CONCEPTs` provides high order FEM, which is very helpful. This advantage is proven by a comparative analysis between commercial FEM solver COMSOL, which does not support high order FEM. We perform high order `CONCEPTs` simulation and compare with COMSOL simulation using second and third order elements. The `CONCEPTs` simulation achieves better results with much less consumption of number of DOFs. It should also be noted that the COMSOL

simulations using third order elements are more efficient than that using second order elements. The comparisons show that for the FEM simulation of the plasmonic scattering problem in layered media, high order elements are more efficient, and therefore should be applied.

The solution is primarily smooth inside the physical domain, but exponentially decaying in the PML domain. Therefore, *hp*-refinement is applied to enhance the computational efficiency. In this paper, we apply non-uniform polynomial orders, and an adaptive mesh refinement towards the PML interface. We have performed intensive simulations by varying the polynomial degrees and level of mesh refinement to study their influence. We observe that the error decays exponentially by increasing the polynomial degrees inside the PML domain or by refining the mesh inside the PML domain towards the PML interface. Moreover, the adaptive mesh refinement is more efficient than increasing the polynomial degrees.

We also learn that there is a saturation level of error, if one only applies mesh refinement or raises polynomial degrees inside the PML. When the saturation level is reached, one can only reduce it further by increasing the polynomial degrees in the physical domain. This phenomenon shows that the saturation level is decided by p_{int}, which corresponds to the modeling error inside the physical domain. The solution is exponential decaying inside the PML domain, therefore adaptive mesh refinement gives better convergence in general. Based on the analysis, an *hp* strategy is developed. The strategy can converge to very high accuracy within very few steps and with a small additional cost of DOFs. We are sure that this strategy can also be applied to more general problems involving PML.

ACKNOWLEDGMENT

The authors acknowledge Xevi Roca, UPC, Spain for help with EZ4U. The authors acknowledge Holger Brandsmeier, ETH Zurich, Switzerland, for the help of `CONCEPTs`. The authors also acknowledge Sascha Schnepp, ETH Zurich, Switzerland, for his valuable suggestions. This work is supported by the Swiss National Science Foundation, under SNSF 119813.

REFERENCES

1. Bharadwaj, P., B. Deutsch, and L. Novotny, "Optical antennas," *Advances in Optics and Photonics*, Vol. 1, No. 3, 438–483, 2009.
2. Novotny, L. and B. Hecht, *Principles of Nano-optics,* Cambridge University Press, 2012.

3. Smajic, J., C. Hafner, and D. Erni, "Design and optimization of an achromatic photonic crystal bend," *Opt. Express*, Vol. 11, No. 12, 1378–1384, 2003.
4. Stewart, M. E., C. R. Anderton, L. B. Thompson, J. Maria, S. K. Gray, J. A. Rogers, and R. G. Nuzzo, "Nanostructured plasmonic sensors," *Chemical Reviews*, Vol. 108, No. 2, 494–521, 2008.
5. Sannomiya, T., C. Hafner, and J. Voros, "In situ sensing of single binding events by localized surface plasmon resonance," *Nano Letters*, Vol. 8, No. 10, 3450–3455, 2008.
6. Sannomiya, T., C. Hafner, and J. Vörös, "Plasmonic nanoparticle based biosensing: Experiments and simulations," *Proc. SPIE, Plasmonics: Nanoimaging, Nanofabrication, and Their Applications V*, Vol. 7395, 73950M, 2009.
7. Kong, J. A., *Electromagnetic Wave Theory,* Wiley, New York, 1986.
8. Ihlenburg, F., *Finite Element Analysis of Acoustic Scattering,* Springer, Berlin & Heidelberg, Germany, 1998.
9. Givoli, D., *Numerical Methods for Problems in Infinite Domains,* Elsevier, Amsterdam and New York, 1992.
10. Bonnet-BenDhia, A.-S., G. Dakhia, C. Hazard, and L. Chorfi, "Diffraction by a defect in an open waveguide: A mathematical analysis based on a modal radiation condition," *SIAM J. Appl. Math.*, Vol. 70, No. 3, 677–693, Jul. 2009.
11. Ciraolo, G. and R. Magnanini, "A radiation condition for uniqueness in a wave propagation problem for 2-D open waveguides," *Math. Meth. Appl. Sci.*, Vol. 32, No. 10, 1183–1206, 2009.
12. Bonnet-BenDhia, A.-S., B. Goursaud, and C. Hazard, "Mathematical analysis of the junction of two acoustic open waveguides," *SIAM J. Appl. Math.*, Vol. 71, 2048–2071, 2011.
13. Jeresz-Hanckes, C. and J.-C. Nédélec, "Asymptotics for Helmoltz and Maxwell solutions in 3-d open waveguides," *Commun. Comput. Phys.*, Vol. 11, No. 2, 629–646, Feb. 2012.
14. Schmidt, F., "A new approach to coupled interior-exterior Helmholtz-type problems: Theory and algorithms," Habilitation Thesis, Free University Berlin, Germany, 2002.
15. Aksun, M. I. and G. Dural, "Clarification of issues on the closed-form Green's functions in stratified media," *IEEE Transactions on Antennas and Propagation*, Vol. 53, No. 11, 3644–3653, 2005.

16. Sauter, S. and C. Schwab, *Boundary Element Methods*, Springer-Verlag, Heidelberg, 2011.
17. Alparslan, A., M. I. Aksun, and K. A. Michalski, "Closed-form Green's functions in planar layered media for all ranges and materials," *IEEE Transactions on Microwave Theory and Techniques*, Vol. 58, No. 3, 602–613, 2010.
18. Alparslan, A. and C. Hafner, "Using layered geometry Green's functions in the multiple multipole program," *Journal of Computational and Theoretical Nanoscience*, Vol. 8, No. 8, 1600–1608, 2011.
19. Berenger, J.-P., "A perfectly matched layer for the absorption of electromagnetic waves," *Journal of Computational Physics*, Vol. 114, No. 2, 185–200, 1994.
20. Jin, J.-M. and W. C. Chew, "Combining PML and ABC for the finite-element analysis of scattering problems," *Microwave and Optical Technology Letters*, Vol. 12, No. 4, 192–197, 1996.
21. Chew, W. C., W. H. Weedon, and A. Sezginer, "A 3-D perfectly matched medium by coordinate stretching and its absorption of static fields," *Applied Computational Electromagnetics Symposium Digest*, Vol. 1, 482–489, Citeseer, 1995.
22. Bermúdez, A., L. Hervella-Nieto, and A. Prieto, "An optimal perfectly matched layer with unbounded absorbing function for time-harmonic acoustic scattering problems," *Journal of Computational Physics*, Vol. 223, No. 2, 469–488, 2007.
23. Collino, F. and P. Monk, "The perfectly matched layer in curvilinear coordinat," *SIAM Journal on Scientific Computing*, Vol. 19, No. 6, 2061–2090, 1998.
24. Zschiedrich, L., R. Klose, A. Schädle, and F. Schmidt, "A new finite element realization of the perfectly matched layer method for Helmholtz scattering problems on polygonal domains in two dimensions," *Journal of Computational and Applied Mathematics*, Vol. 188, No. 1, 12–32, 2006.
25. Chen, Z. and H. Wu, "An adaptive finite element method with perfectly matched absorbing layers for the wave scattering by periodic structures," *SIAM J. Numer. Anal.*, Vol. 41, No. 3, 799–826, 2003.
26. Bao, G., Z. Chen, and H. Wu, "Adaptive finite-element method for diffraction gratings," *JOSA A*, Vol. 22, No. 6, 1106–1114, 2005.
27. Michler, C., L. Demkowicz, J. Kurtz, and D. Pardo, "Improving the performance of perfectly matched layers by means of *hp*-adaptivity," *Numerical Methods for Partial Differential Equations*,

Vol. 23, No. 4, 832–858, 2007.

28. Zschiedrich, L., "Transparent boundary conditions for Maxwell's equations," Ph.D. Thesis, FU Berlin, Berlin, Germany, Nov. 2009.
29. Nannen, L. and A. Schädle, "Hardy space infinite elements for Helmholtz-type problems with unbounded inhomogeneities," *Wave Motion*, Vol. 48, No. 2, 116–129, 2011.
30. Kettner, B. and F. Schmidt, "The pole condition as transparent boundary condition for resonance problems: Detection of spurious modes," *Proc. SPIE*, Vol. 7933, 79331B-1–79331B-11, 2011.
31. Kettner, B., "Detection of spurious modes in resonance mode computations — Pole condition method," Ph.D. Thesis, FU Berlin, Berlin, Germany, Jul. 2012.
32. Schwab, C., *p- and hp-finite Element Methods: Theory and Applications in Solid and Fluid Mechanisms*, Oxford University Press, Oxford, UK, 1998.
33. Ainsworth, M., "Discrete dispersion relation for *hp*-version finite element approximation at high wave number," *SIAM J. Numer. Anal.*, Vol. 42, No. 2, 553–575, 2005.
34. Melenk, J. M. and S. Sauter, "Convergence analysis for finite element discretizations of the Helmholtz equation with Dirichletto-Neumann boundary conditions," *Math. Comp.*, Vol. 79, No. 272, 1871–1914, 2010.
35. Melenk, J. M. and S. Sauter, "Wavenumber explicit convergence analysis for Galerkin discretizations of the Helmholtz equation," *SIAM J. Numer. Anal.*, Vol. 49, No. 3, 1210–1243, 2011.
36. Babuška, I. and B. Q. Guo, "Approximation properties of the *h-p* version of the finite element method," *Computer Methods in Appl. Mechanics Engineering*, Vol. 133, 319–346, 1996.
37. Schmidt, K. and P. Kauf, "Computation of the band structure of two-dimensional photonic crystals with *hp* finite elements," *Computer Methods in Appl. Mechanics Engineering*, Vol. 198, 1249–1259, Mar. 2009.
38. Babushka, I. and W. Rheinbolt, "A posteriori analysis for adaptive finite element computations," *SIAM J. Numer. Anal.*, Vol. 15, 736–754, 1978.
39. Ainsworth, M. and J. T. Oden, "A posteriori error estimation in finite element analysis," *Computer Methods in Appl. Mechanics Engineering*, Vol. 142, Nos. 1–2, 1–88, 1997.
40. Ainsworth, M. and B. Senior, "An adaptive refinement strategy for *hp*-finite element computations," *Appl. Numerical Mathematics*, Vol. 26, 165–178, 1998.

41. Becker, R. and R. Rannacher, "An optimal control approach to a posteriori error estimation in finite element methods," *Acta Numerica*, Vol. 10, No. 1, 1–102, 2001.
42. Demkowicz, L., *Computing with hp-adaptive Finite Elements: One and Two Dimensional Elliptic and Maxwell Problems,* Chapman and Hall/CRC Applied Mathematics and Nonlinear Science, 2006.
43. Schnepp, S. M. and T. Weiland, "Efficient large scale electromagnetic simulations using dynamically adapted meshes with the discontinuous Galerkin method," *Journal of Computational and Applied Mathematics*, Vol. 236, No. 18, 4909–4924, 2011.
44. Wihler, T. P., "An *hp*-adaptive strategy based on continuous Sobolev embeddings," *Journal of Computational and Applied Mathematics*, Vol. 235, No. 8, 2731–2739, 2011.
45. Bürg, M. and W. Döfler, "Convergence of an adaptive *hp* finite element strategy in higher space-dimensions," *Applied Numerical Mathematics*, Vol. 61, No. 11, 1132–1146, 2011.
46. Jackson, J. D., *Classical Electrodynamics,* 3rd Edition, John Wiley & Sons, 1999.
47. Fang, Y., N.-H. Seong, and D. D. Dlott, "Measurement of the distribution of site enhancements in surface-enhanced Raman scattering," *Science*, Vol. 321, No. 5887, 388–392, 2008.
48. Park, S. J. and R. E. Palmer, "Acoustic plasmon on the Au (111) surface," *Physical Review Letters*, Vol. 105, No. 1, 016801, 2010.
49. Pohl, K., B. Diaconescu, G. Vercelli, L. Vattuone, V. M. Silkin, E. V. Chulkov, P. M. Echenique, and M. Rocca, "Acoustic surface plasmon on Cu (111)," *EPL (Europhysics Letters)*, Vol. 90, No. 5, 57006, 2010.
50. Vattuone, L., M. Smerieri, T. Langer, C. Tegenkamp, H. Pfnür, V. M. Silkin, E. V. Chulkov, P. M. Echenique, and M. Rocca, "Correlated motion of electrons on the Au (111) surface: Anomalous acoustic surface-plasmon dispersion and single-particle excitations," *Physical Review Letters*, Vol. 110, No. 12, 127405, 2013.
51. Vattuone, L., G. Vercelli, M. Smerieri, L. Savio, and M. Rocca, "Acoustic surface plasmon dispersion on nanostructured Cu (111)," *Plasmonics*, Vol. 7, No. 2, 323–329, 2012.
52. Politano, A., G. Chiarello, V. Formoso, R. G. Agostino, and E. Colavita, "Plasmon of shockley surface states in Cu (111): A high-resolution electron energy loss spectroscopy study," *Physical Review B*, Vol. 74, No. 8, 081401, 2006.

53. Politano, A., "Low-energy collective electronic mode at a noble metal interface," *Plasmonics*, Vol. 8, No. 2, 357–360, 2013.
54. Schmidt, K. and R. Kappeler, "Efficient computation of photonic crystal waveguide modes with dispersive material," *Optics Express*, Vol. 18, No. 7, 7307–7322, 2010.
55. Frauenfelder, P. and C. Lage, "Concepts — An object-oriented software package for partial differential equations," *ESAIM: Mathematical Modelling and Numerical Analysis*, Vol. 36, No. 05, 937–951, 2002.
56. Ramos, J. S. and A. Huerta, "Efficient unstructured quadrilateral mesh generation," *International Journal for Numerical Methods in Engineering*, Vol. 49, 1327–1350, 2010.
57. EZ4U, Mesh Generation Environment, www.lacan.upc.edu/ez4u.htm.
58. Hafner, C., *MaX-1: A Visual Electromagnetics Platform for PCs,* John Wiley & Sons, Chichester, UK, 1999.
59. Hafner, C., *Post-modern Electromagnetics: Using Intelligent Maxwell Solvers,* Wiley, 1999.
60. Alparslan, A. and C. Hafner, "Analysis of photonic structures by the multiple multipole program with complex origin layered geometry Green's functions," *Journal of Computational and Theoretical Nanoscience*, Vol. 9, No. 3, 479–485, 2012.
61. COMSOL Multiphysics, http://www.comsol.com/.